Process optimization and characterization of dense pure copper parts produced by paste-based 3D micro-extrusion

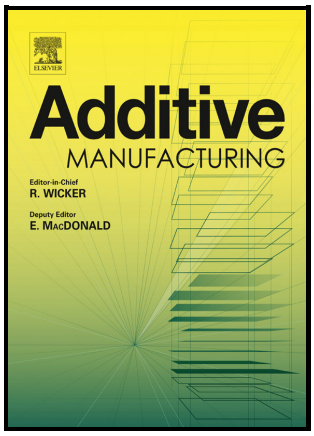

Margherita Beretta, Samanwitha Kolli, Ahmed Selema, Peter Sergeant, Leo A.I. Kestens, Marleen Rombouts, Jozef Vleugels

PII: S2214-8604(23)00283-X

DOI: https://doi.org/10.1016/j.addma.2023.103670

Reference: ADDMA103670

To appear in: *Additive Manufacturing*

Received date: 11 April 2023
Revised date: 6 June 2023
Accepted date: 23 June 2023

Please cite this article as: Margherita Beretta, Samanwitha Kolli, Ahmed Selema, Peter Sergeant, Leo A.I. Kestens, Marleen Rombouts and Jozef Vleugels, Process optimization and characterization of dense pure copper parts produced by paste-based 3D micro-extrusion, *Additive Manufacturing,* (2023) doi:https://doi.org/10.1016/j.addma.2023.103670

Process optimization and characterization of dense pure copper parts produced by paste-based 3D micro-extrusion

Authors: Margherita Beretta [a,b,1], Samanwitha Kolli [a,c,*,1], Ahmed Selema [b,d], Peter Sergeant [b,d], Leo A.I. Kestens [b], Marleen Rombouts [c,2], Jozef Vleugels [a,2]

[a] Department of Materials Engineering, KU Leuven, Kasteelpark Arenberg 44, B-3001 Heverlee, Belgium
[b] Department of Electromechanical, Systems, and Metal Engineering, Ghent University, B-9052 Ghent, Belgium
[c] Coating and Shaping Technologies group, Flemish Institute for Technological Research – VITO NV, Boeretang 200, B-2400 Mol, Belgium
[d] FlandersMake@UGent, Core Lab EEDT-MP, B-3001 Leuven, Belgium

*Corresponding author.
E-mail address: samanwitha.kolli@kuleuven.be (Samanwitha Kolli)
[1]Joint first authors – These authors contributed equally to this paper
[2]Joint senior authors

Abstract

The manufacturing of dense pure Cu components by 3D micro-extrusion, a Material Extrusion (MEX) Additive Manufacturing (AM) technology, was investigated. This technology is based on the extrusion of a highly viscous powder-loaded suspension or paste at room temperature. The present study focused on the development of a complete processing route for 3D micro-extrusion from feedstock paste formulation, optimization of printing parameters, and thermal post-processing conditions. A propanol-based feedstock paste with 95 wt% Cu powder loading was prepared by employing optimized mixing and degassing steps to produce ~98% dense Cu after pressureless sintering in pure H_2 atmosphere at 1050 °C for 5 hours. Printing of green parts by 3D micro-extrusion of the developed paste with optimized printing parameters followed by the same post-processing conditions enabled the fabrication of 96-99% dense Cu components with high purity. Microstructural investigation of the paste and printed parts after thermal treatment revealed the presence of residual isolated spherical pores (<10 µm) distributed within the grains, at the grain boundaries and in triple junctions. The final material has an electrical conductivity in the range 90-100 %IACS, a yield strength of 61 ± 7 MPa, an ultimate tensile strength of 194 ± 9 MPa and an elongation at fracture of 32 ± 4 %.

1. Introduction

Increasing the energy efficiency of thermal management devices and electrical machines is drawing increasing attention in the view of sustainable development [1,2]. Two important elements that govern the performance of these components are 1) the choice of high-performance materials which can maximize energy transfer, and 2) the adoption of a flexible and effective manufacturing technology that allows to achieve an optimal design [3]. Pure copper, owing to its outstanding thermal and electrical conductivity properties, represents a suitable candidate for energy management systems [4]. Apart from the functional properties of Cu, the performance of such devices is remarkably affected by their geometry. The optimization of the surface area to volume ratio enables maximum heat transfer which is achieved by introducing complex features into heat exchangers [5]. Similarly, in electrical machines, one of the crucial factors is the design of the conductor profile that enables a reduction in current losses [3]. The flexibility to build complex geometrical features and customizability to meet specific

application requirements is limited in conventional manufacturing routes. In this regard, additive manufacturing (AM), in view of its high fabrication freedom and ability to produce smaller and lighter parts with enhanced performance, is rapidly gaining industrial consideration.

Amongst the various AM techniques, laser powder bed fusion (LPBF) is most developed and employed for the fabrication of a wide range of metallic components. However, due to the intrinsic properties of copper such as high optical reflectivity and thermal conductivity, fabrication of high-quality dense parts by LPBF is reported to be challenging [4]. The process requires high power laser sources that could damage the equipment [6], expensive lasers such as green laser [7], or powder modification by addition of alloying elements to improve the absorptivity of the laser [8]. Nevertheless, few studies have reported pure copper parts with final relative density >98 % of the theoretical density (TD) and electrical conductivity in the range of 76-96 %IACS (International Annealed Copper Standard) [6,9–11]. Qu et al. achieved an electrical conductivity of 76 %IACS for as-built Cu parts with a relative density of 99.6 %TD, produced via high-precision LPBF with optimized printing parameters for densification. The lower electrical conductivity was attributed to the resultant fine grain size, high dislocation density, and defects. A subsequent thermal treatment at 1000 °C for 12 hours promoted grain growth and improved the conductivity to 96 %IACS [9]. Jadhav and Goossens et al. reported on the production of 99.3% dense pure Cu parts fabricated through LPBF with an electrical conductivity of 94 %IACS. The 5-6 %IACS reduction in the as-built parts was assumed to be due to the presence of impurities in the range of 100-200 ppm, a residual porosity of 0.7%, measuring in the direction perpendicular to printing, fine grain structure, and high dislocation density. On the other hand, electron beam melting (EBM) allowed the production of 99.95% dense parts [12–14] with an electrical conductivity of 96.24% [12]. Guschlbauer et al. demonstrated a high dependence of the electrical conductivity of EBM bulk Cu on the purity of the starting powders. The use of pure copper powder with impurities below 2 ppm enabled the manufacturing of components with electrical conductivity over 100 %IACS. The EBM parts exhibited strong anisotropy with respect to the building direction. Moreover, process-induced cracks due to internal stresses were detected on the fracture surface of tensile parts [14].

The processing challenges related to direct (single-step) AM of pure Cu form a motivation to explore indirect (multi-steps) AM technologies such as binder jetting, ultrasonic-assisted AM, and extrusion-based 3D printing or material extrusion (MEX). These techniques offer the processability of a wide range of materials (ceramics and metals) since they involve printing and post-processing (debinding and sintering) in two separate steps. Binder jetting (BJ) of pure Cu has been explored by Bai et al., who manufactured parts with a maximum of 85.5 %TD upon sintering at 1080 ^{o}C for 4 h with a volumetric shrinkage of 43.4% [15]. In a later study, the same research group has reported that the relative density of the part could be improved from 90.5 %TD, for the as-sintered condition showing closed isolated porosity, up to 97.3 %TD by subsequent hot isostatic pressing (HIP) [16]. This additional step enabled to achieve an electrical and thermal conductivity of 96.6 %IACS and 327.9 W/m.K respectively. The work also demonstrated improved mechanical properties and electrical conductivity with higher density. Singh et al. explored AM of dense Cu by employing an ultrasonic-assisted technology and could produce parts with a maximum of 90 %TD [17].

In contrast to the two aforementioned powder bed-based indirect AM technologies, MEX is an evolving AM technology that allows the selective deposition of feedstock layer-by-layer followed by densification. MEX technologies can be distinguished according to the type of feedstock, i.e. filament, pellet/granules, or paste. Few studies attempted the production of pure Cu by extrusion-based AM of a filament feedstock such as Fused Deposition Modeling (FDM) [18] and Fused Filament Fabrication (FFF) [19–21]. Cañadilla et al. studied FFF of pure copper and have demonstrated the feasibility of

producing parts of 95.3 %TD using Markforged® filament containing 95 wt% metal which exhibited an electrical conductivity of 82 %IACS [21]. Regarding MEX using pellet-based feedstock, Ren et al. tested multiple sintering temperatures for the densification of the parts. A maximum relative density of only 91 %TD was achieved with significantly inferior electrical conductivity (~15 %IACS) than wrought Cu (~102 %IACS) despite sintering at a sintering temperature close to 1083 °C [22]. Singh et al. reported on the fabrication of pure copper parts using MIM feedstock pellets of 93.5 wt% solid loading, allowing to obtain 91 %TD [23]. Further adjustment of the printing parameters and sintering conditions to 1050 °C/3h in He-4%H_2 atmosphere enabled a maximum densification to 94.5 %TD with an isotropic shrinkage of ~13.1% [23]. MEX using a highly powder-loaded paste, also known as 3D micro-extrusion or robocasting, has been studied by Danaci et al. for the production of copper scaffold support structures for catalytic applications [24]. Few studies focused on the manufacturing of dense Cu parts by paste-based MEX followed by pressureless sintering with a maximum relative density achieved of 90 %TD [25,26]. Yan et al. printed a Cu paste formulated with 99.5% pure Cu powder (average size of 1µm) and paraffin wax as a binder. They reported a maximum density of only 90 %TD upon sintering at 1000 °C. The purity of the final sintered parts by complete binder burnout was demonstrated using energy dispersive spectroscopy (EDS) point analysis where the spectrum showed no carbon peak [25]. Hong et al. explored the feasibility of producing Cu parts using a paste, containing polyvinyl carboxy polymer and polyvinyl alcohol as a rheology modifier, by studying the influence of metal powder loading on the viscosity of the Cu paste. A sintering shrinkage of 23% was reported for the parts manufactured with the highest Cu content (82 wt%), but no density values were mentioned [26].

As a contribution to AM of Cu, the present study focuses on the development of a processing route to produce high-purity dense copper components by paste-based 3D micro-extrusion. This includes in-house development of a high Cu powder load feedstock paste followed by a comprehensive characterization (thermal, rheological, and chemical analysis), optimization of the printing parameters, and assessment of the sintered material properties (physical, chemical, functional, and mechanical). For the first time, the manufacturing of highly dense (96-99 %TD) and conductive (100 %IACS) Cu components by 3D micro-extrusion of a highly loaded paste at room temperature followed by pressureless sintering was demonstrated.

2. Experimental procedure

The fabrication and characterization of dense Cu parts were performed in five steps: (i) copper feedstock paste preparation, (ii) 3D micro-extrusion of green parts, (iii) drying, (iv) thermal debinding and sintering, and (v) characterization - density, electrical conductivity, and static tensile properties.

2.1 Feedstock materials and paste preparation

Gas atomized pure Cu powder (Safina, particle size < 15 µm) was used. The Particle Size Distribution (PSD) was assessed using a LS 13 320 particle size analyzer (Beckman Coulter™) whereas the morphology of the particles was characterized by scanning electron microscopy (SEM, XL30 FEI). X-ray fluorescence analysis (XRF) of the powder was performed using a wavelength dispersive spectrometer (Bruker S8 TIGER 4K). From the PSD analysis, the d10, d50, and d90 were measured to be 3.9 µm, 10.7 µm, and 17.9 µm respectively (Figure 1b). SEM imaging revealed that the shape of the starting powder particles was mainly spherical with the presence of finer satellites on the coarser

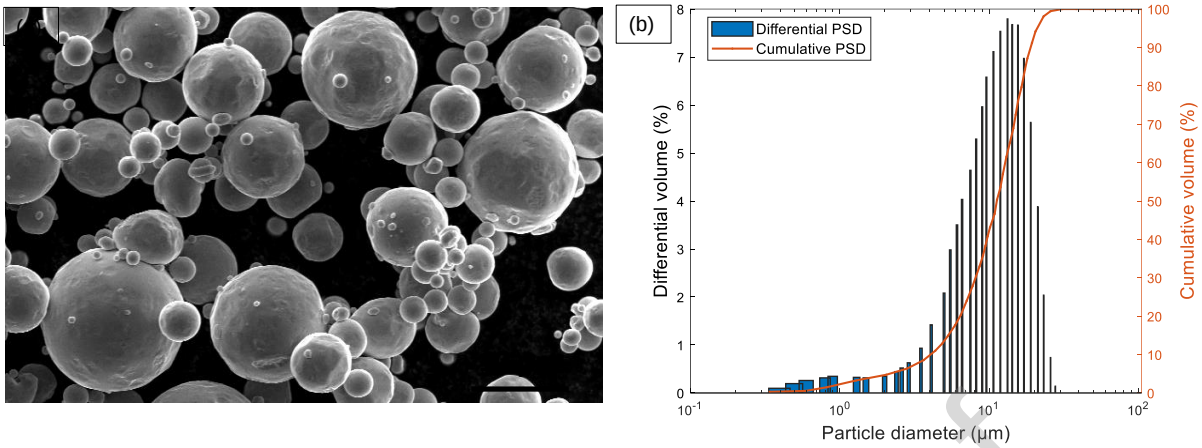

Figure 1: (a) SEM micrograph (b) and particle size distribution (PSD) of the Cu starting powder employed for 3D micro-extrusion.

particles (Figure 1a). The XRF analysis revealed only Fe (~100 ppm) as impurity in the Cu powder. The true density of the starting powder (which is considered as the theoretical density, TD) was measured to be 8.91 g/cm^3 using a Multipycnometer™ (Quantachrome Instruments).

A binder solution of hydroxypropyl cellulose (HPC) in 1-propanol was used with other organic additives for lubrication. Two binder compositions were chosen to comprehend the printability and green strength of the parts: 2 wt% HPC of 1.000.000 Molecular Weight (Sigma Aldrich) and 4 wt% HPC of 370.000 Molecular Weight (Sigma Aldrich) in 1-propanol (Sigma Aldrich). The final composition of the feedstock pastes with the solid loading, binder and lubricant content is reported in Table 1.

The paste is prepared by planetary-centrifugal mixing the raw material using a speedmixer (Hauschild Speedmixer DAC1100) at atmospheric pressure followed by a degassing step, i.e. mixing in vacuum in the same speedmixer. The mixing and degassing cycle parameters were chosen as a tradeoff between the achievement of a uniform homogeneous paste with minimal entrapped air, avoidance of phase separation and temperature rise of the paste that promotes solvent evaporation. A study on mixing and degassing was performed by characterizing the sintered paste in an as-mixed and degassed state and is discussed in later sections. The feedstock paste was transferred to a syringe which is connected to the printing head.

Rheological measurements (Mars 60, Thermo Fisher Haake) of the 2HPC and 4HPC pastes were carried out at room temperature using a parallel plate geometry of 35 mm diameter with a 0.4 mm gap height.

Table 1 Feedstock paste formulations prepared for the manufacturing of pure Cu parts by 3D micro-extrusion.

Feedstock paste	**2HPC** 2 wt% HPC + 1-propanol		**4HPC** 4 wt% HPC + 1-propanol	
	wt%	vol%	wt%	vol%
Cu powder	94.73	61.95	94.81	62.42
Binder	4.49	32.99	4.36	32.63
Lubricant	0.78	5.07	0.76	4.94

Rotational flow sweeps were conducted at shear rates of 0.01 – 100 s^{-1} and the oscillatory amplitude sweep stress-controlled measurements were conducted with an oscillation stress varying in the range of 1 Pa to 10^4 Pa at a frequency of 1 Hz. All measurements were performed using a solvent trap to minimize the drying of the paste.

2.2 Printing

3D micro-extrusion was carried out using a 3Dn-450HP n-Scrypt high-precision printer. The 3D printer comprises a needle-type extrusion system integrated with a smart pump and valve body with a valve rod. On application of compressed air from one end of the syringe, the smart pump system (as described in Figure 2) allows a controlled flow rate of the paste governed by the ascending and descending positions of the valve rod. The paste is extruded as a single fiber when the valve rod descends, opening the valve body (open position), whereas the paste flow ceases when the valve rod rises closing the valve body (closed position). Before printing the parts, the feedstock paste was extruded into single fibers (referred to as 'paste fibers') of ~2 mm diameter directly from the syringe mounted on the printer as depicted in Figure 3b. Structural and microstructural characterization was performed on the sintered fibers in order to compare them to the sintered 3D printed parts. During the process of printing, the highly viscous paste was extruded through a fine nozzle (400 or 580 µm diameter) and deposited layer-by-layer at room temperature adapting to the given CAD design (Figure 3c). Parts of three different dimensions were printed: 20x20x3.5 mm^3 and 35x35x5 mm^3 (cuboid) and 80x15x3.5 mm^3 (bar) to evaluate density, electrical conductivity and mechanical properties after sintering, employing the optimized printing parameters as listed in Table 3. The printed parts were dried at controlled temperature (~20 °C) before subsequent processing.

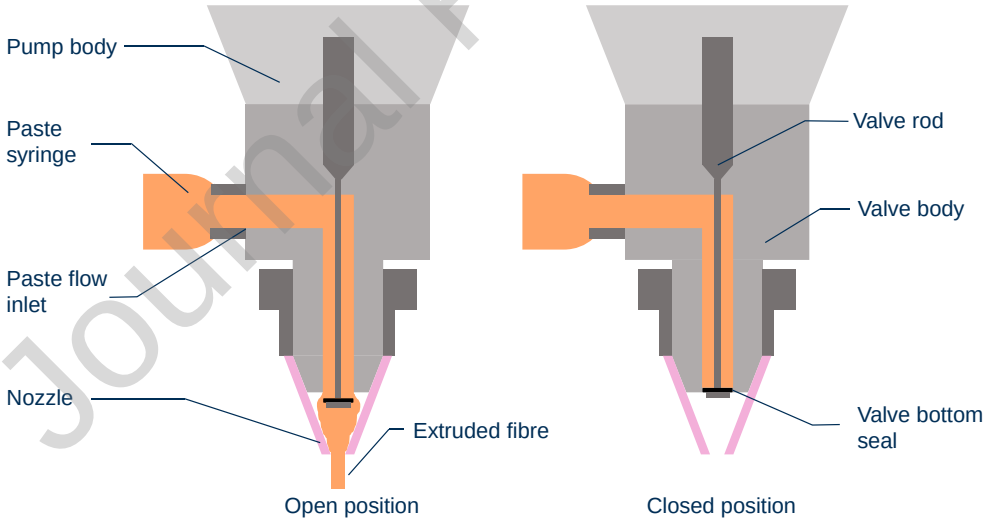

Figure 2 Schematic representation of the smart pump system in the open (left) and close position (right) configurations.

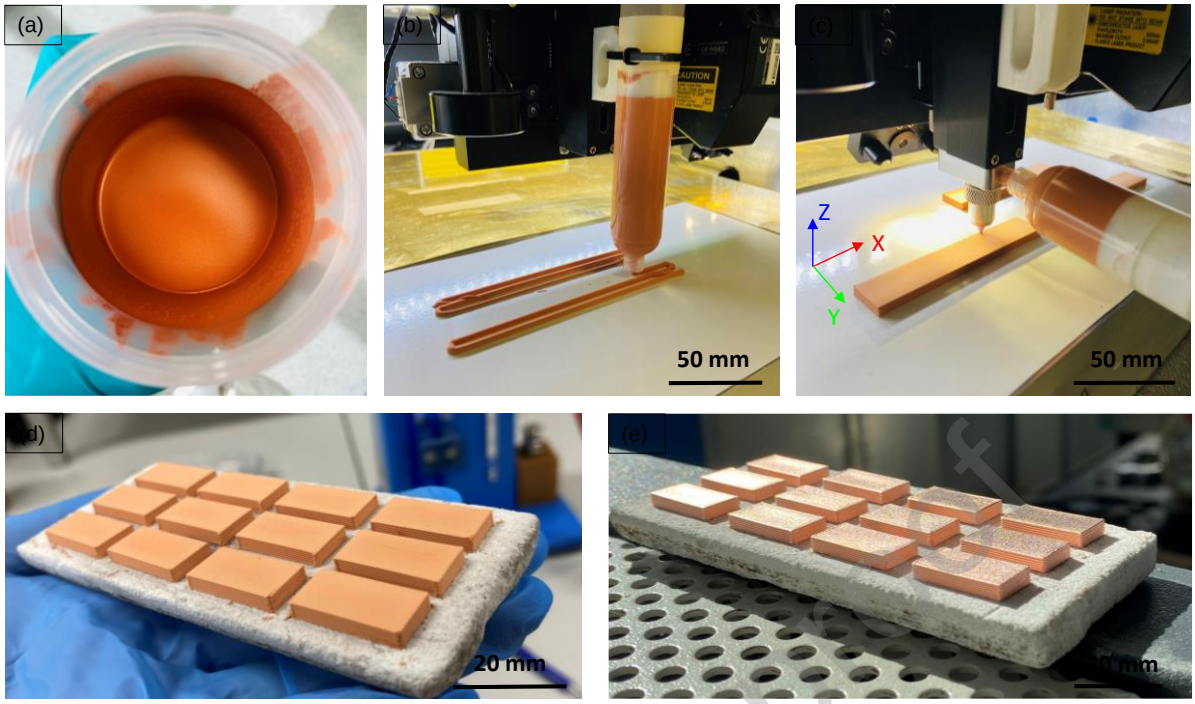

Figure 3 3D micro-extrusion process chain consisting of: (a) the preparation of Cu feedstock paste, (b) controlled extrusion of a single fiber, (c) printing of the parts that are subsequently (d) dried and (e) debound and sintered.

Printing by 3D micro-extrusion technology involves optimization of various printing parameters such as nozzle diameter, printing speed, extrusion pressure, and printing strategy that includes fiber spacing, layer thickness, and fiber orientation. The nozzle diameter is constrained by the maximum particle diameter of the starting powder: to ensure a smooth extrusion it has to be at least 5 to 10 times larger than the biggest particle [27]. Considering the PSD of the starting Cu powder, dimensional accuracy and productivity, nozzle diameters of 400 and 580 µm were chosen. An appropriate infill can be realized by choosing an optimal ratio between printing speed and mass flow rate which depends on the extrusion air pressure and valve rod position[28]. For the parts shaped in this work, an extrusion air pressure of 0.139 - 0.152 MPa was employed relative to the printing speed of 20 mm/s. Another important set of parameters is the printing strategy or layer stacking. Research on extrusion-based printing has been performed by employing various printing strategies, i.e. cross-printing [21], [23], unidirectional [29] and unidirectional (0-0°) hexagonal layer stacking [30]. Feilden et al. employed a hexagonal layer stacking which is anticipated to result in a closed-packed stacking of filaments along with an overlap of the fibers [30]. Therefore, unidirectional hexagonal stacking with an additional overlap between the extruded fibers was adopted in the present work to take advantage of the highest possible packing as shown in Figure 4. A similar strategy of employing overlap of the fibers with a novel approach was proposed by Côté et al. demonstrating it to be more effective than the commonly employed over-extrusion or flow multiplier approach to eliminate interbead defects and obtain dense green parts[29]. In this study, the impact of scan spacing and layer thickness on the final density has been investigated whilst leaving other printing parameters unchanged. The study was performed by printing parts with a broad range of scan spacings (SP - 350, 300, 250 µm) and layer thicknesses (LT - 200, 225, 250, 300 µm) using a 400 µm nozzle diameter.

Figure 4 Schematic representation of possible printing strategies during printing of dense parts using 3D micro-extrusion: unidirectional stacking (left), unidirectional hexagonal stacking (centre) and unidirectional hexagonal stacking with overlap of the fibers and lower layer thickness that was adopted in this study (right).

2.3 Debinding and sintering

The investigation of the proper debinding conditions was carried out by performing thermogravimetric analysis TGA (SDT Q600, TA Instruments) on a dried green Cu fiber sample with a heating rate of 10°C/min up to 600 °C in pure Ar gas (Liquid Argon >99.998% , $O_2 \leq$ 1.5 ppm, Nippon Gases NV). The weight variation measured on the dried paste during thermogravimetric analysis corresponded to the loss (in weight %) of organic additives that were burned out during heating as shown in Figure 5. Since the maximum weight loss occurred at 500 °C, a debinding temperature of 550 °C was considered optimal for the debinding step. Whereas, the sintering temperature was chosen with respect to preliminary studies and with reference to the literature where Singh et al. reported 1050°C/3h to be an optimal sintering temperature in a reducing atmosphere (4%H_2) [23]. Therefore, in the present study, the dried printed parts were debound at 550 °C for 5h with a heating rate of 0.5 °C/min in 95% Ar+5% H_2 atmosphere with a flow rate of 30 L/h (Alphagaz Mix H_2 5%/Ar, $O_2 \leq$ 5 ppm, Air Liquide). This was followed by pressureless sintering at 1050 °C for 5h with a heating rate of 2 °C/min in pure H_2 with a flow rate of 70 L/h (Hydrogen N40 ≥99.99%, $O_2 \leq$ 3 ppm v/v, AirLiquide).

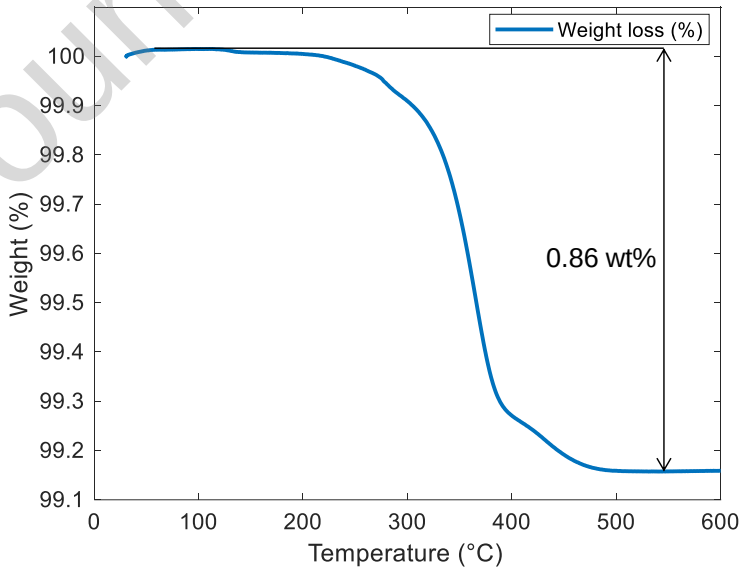

Figure 5 Thermogravimetric analysis (TGA) performed on the dried Cu feedstock paste to assess the amount of weight loss corresponding to the organic content burnout.

A relatively slow heating ramp of 2 °C/min in combination with pure hydrogen atmosphere during sintering was chosen to maximize the reduction of copper oxide to pure copper. Finally, the parts were cooled down to room temperature with cooling rate of 5 °C/min employed the same conditions of debinding step. The entire post-processing thermal treatment consisting of both the debinding and pressureless sintering was performed in a horizontal tube furnace (Carbolite, model: CTF 12/65 equipped with a Eurotherm temperature control).

2.4 Characterization

The green strength of the printed components using the two different binder compositions was evaluated by 3-point bending tests (span width of 25 mm) using an Instron 5943 machine. The dimensions of the samples (32x6.5x13 mm^3) were chosen in accordance with ASTM B312 and were tested after 9 days of drying time at a crosshead displacement of 500 µm/min.

The density of all sintered materials was measured in ethanol according to the Archimedes method with a precision balance (Quintix 224-1S, Sartorius). The true density (TD) of the Cu powder was used for the calculation of the relative density (%TD) of the printed samples. For microstructural investigation, samples were cross-sectioned using a slow-speed cutting machine (Secotom-10, Struers) along the printing and building directions and subsequently cross-section polished with Ar ions (IB-09010CP, Jeol). The characterization was performed using a scanning electron microscope (SEM, XL30 FEI). The analysis of the sintered paste fiber samples was carried out along the longitudinal direction by grinding the surface manually with 800 and 1200 SiC papers prior to polishing with 3 µm and 1 µm diamond suspensions. The visualization and quantitative evaluation of the pores was performed by means of optical microscopy OM (Keyence 3-D Digital Microscope).

Chemical analysis of the starting powder as well as sintered parts was performed by instrumental gas analysis (EAG Laboratories, France) to evaluate the concentration of C, O, H and N.

Two complementary methods were employed to evaluate the electrical conductivity of the sintered parts. For cuboid samples, the electrical conductivity was evaluated through the conductivity probe (Hocking Autosigma) measurement. Whereas for bar specimens, a 4-terminal sensing or 4-point contact method (Kelvin connection) was used to measure the resistance and thereby evaluate the electrical conductivity along the printing direction. A schematic of the 4-terminal connection is shown in Figure 6. As can be seen, the test sample is connected in series with power resistor to limit the current. The voltage and current were simultaneously measured and monitored through a data acquisition system (DAQ, DSP MicroLabBox). A variable DC supply, which can provide a DC current up 110A, was used along with voltage and current probes to measure the instantaneous waveforms. A current amplifier (Tektronix TCPA300) is used to measure the DC current in the test sample. Also, a high-sensitivity differential probe (TT-SI 8052) with a DC accuracy of ±2% is used to measure the voltage drop and export the signal to the DAQ. To ensure a detectable voltage drop, a high current of 100A was injected to the test sample for a very short time interval. The voltage drop is measured in less than 2 seconds at the room temperature to make sure that the sample does not heat up. Finally, the conductivity calculated in S/m based on parts dimensions was then converted into %IACS, which is the relative value calculated with respect to the International Annealed Copper Standard (i.e. 5.8×10^7 S/m at 20 °C which is equivalent to 100 %IACS [31]). In order to reduce the impact of surface roughness, all conductivity measurements were performed on surface machined (milled) sintered bars.

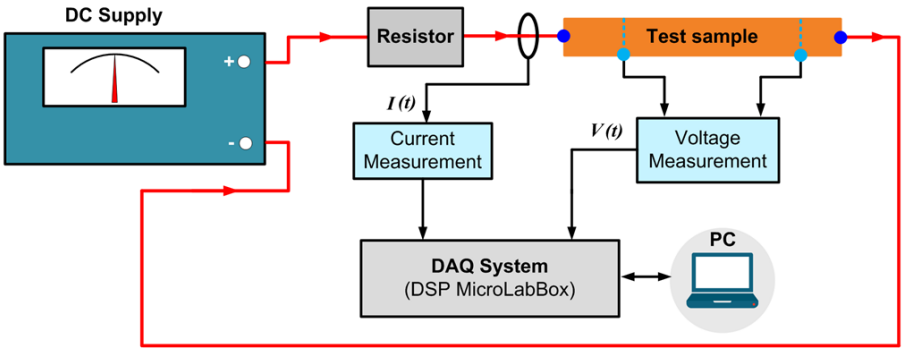

Figure 6 Schematic for the 4-terminal sensing connection to measure the resistance of a copper sample.

The mechanical properties were measured by non-destructive and destructive methods. The Young's modulus (E-modulus) was measured on the surface machined printed bars using the impulse excitation technique (IET, MK7, GrindoSonic) at room temperature, according to ASTM E1876-01 [8]. The bars were finally machined to dog-bone shaped tensile samples in accordance with ISO 6892. Tensile tests were performed parallel to the printing direction using an Instron universal testing machine with a cross-head speed of 0.5 mm/min and an extensometer of 12.5 mm gauge length. Micro-Vickers hardness of the parts was measured with an indentation load of 0.3 kg for 15 sec.

3. Results and discussion

3.1 Feedstock paste characterization

3.1.1 Mixing and degassing

In 3D micro-extrusion, the intrinsic densification behavior of the produced feedstock pastes largely influences the density of the final component, apart from the printing step. Besides the right choice of raw materials, the mixing procedure plays a major role on the packing density and homogeneity of the paste. Figure 7a and b show the optical images of cross-sectioned sintered paste fibers in the as-mixed state and after degassing respectively. The as-mixed condition revealed the presence of a total porosity of ~8.22 % with closed spherical micrometer-sized pores (40-180 µm) along with distributed pores throughout the fiber. These spherical porosities are attributed to entrapped air. Although centrifugal mixing involves de-aeration, it only helps in removing air bubbles that are large enough (few hundreds of micrometers) while the micrometer-sized pores prevail. The spherical pores present in the as-mixed paste were also visualized in the higher magnification SEM cross-section images (Figure 7c and e). On the other hand, an additional degassing step performed at 200 mbar absolute pressure enabled the achievement of a denser paste with uniformly distributed closed residual pores of less than 15 µm accounting for a total porosity of ~3.4 %, as depicted by the overview optical image in Figure 7b. The cross-section of the degassed and sintered fiber is shown in Figure 7d and f. The higher magnification images highlight the presence of isolated residual pores inside the grains and at the grain boundaries. The isolated pores inside the grains inhibit further densification of the paste and thus of the printed parts.

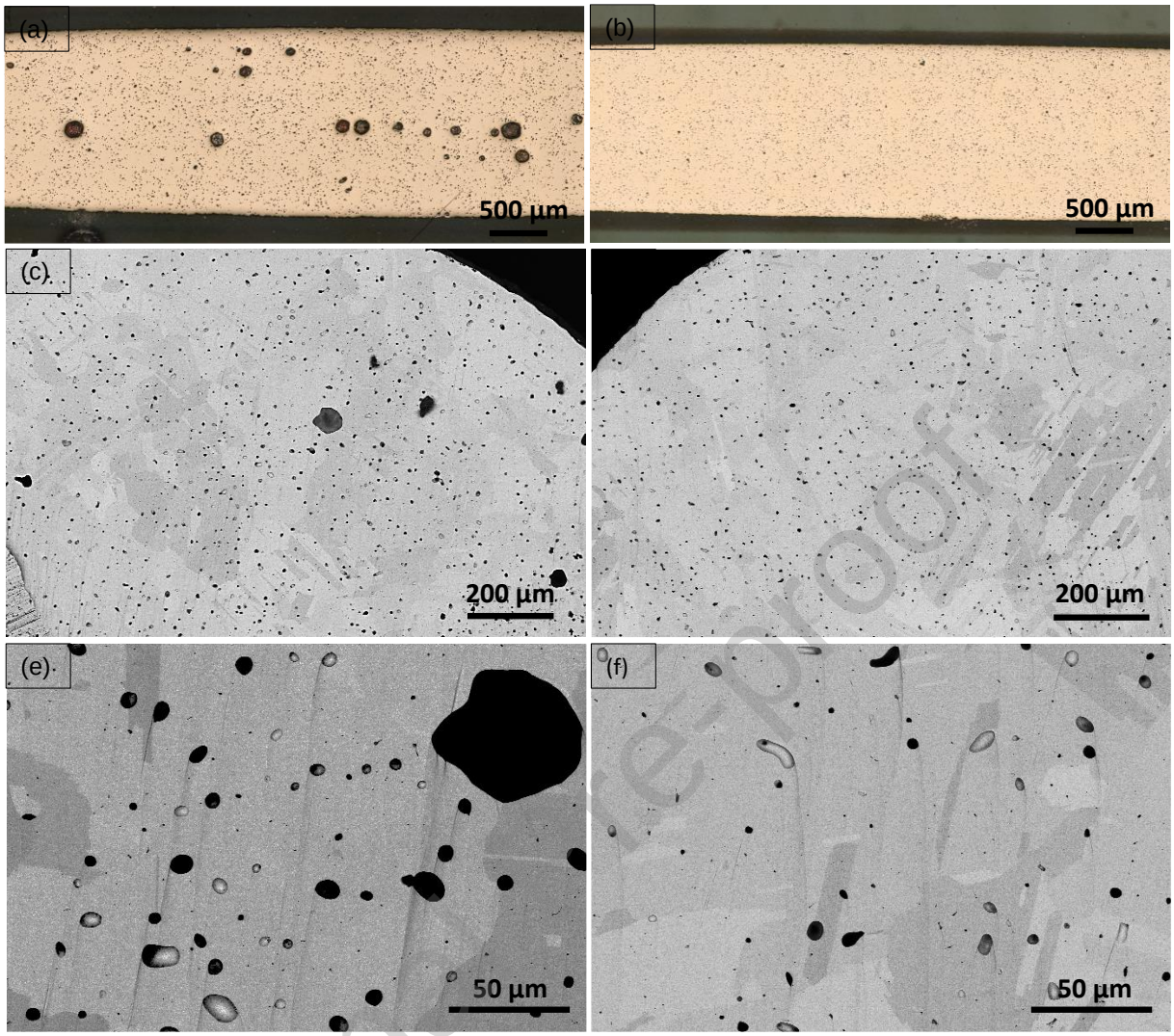

Figure 7 Optical microscopy images of the longitudinal section of as-mixed (a) and degassed (b) Cu feedstock paste fibers after sintering at 1050°C/5h in pure hydrogen. The SEM micrographs of the Ar ion cross-section polished fibers highlights the presence of isolated porosity distributed inside the grains and at the grain boundaries for both as-mixed (c, e) and degassed (d, f) fibers.

3.1.2 Rheology

One of the crucial aspects of the 3D micro-extrusion process is controlling the rheological properties of the feedstock paste to optimize the printability and shape retention of the printed part. A feedstock paste should exhibit a characteristic rheological behavior that ensures a smooth flow through the nozzle during extrusion on the one hand and that retains the as-deposited shape on the other hand. During the 3D micro-extrusion process, the paste experiences high shear rates in the nozzle while zero shear rate on deposition. Therefore, the paste should exhibit shear thinning behavior showing lower viscosity in the nozzle and high viscosity on deposition to retain the shape [32]. Figure 8a shows the rheological behaviour of the feedstock pastes, 2HPC and 4HPC, illustrating the suitable shear thinning and thus depicting good printability. The higher viscosity of the 4HPC than 2HPC paste could be attributed to the higher copper powder loading. The oscillatory measurements in Figure 8b highlight the behavior of the two pastes on the application of dynamic shear stress in terms of moduli and the linear viscoelasticity limits. At a lower stress range, the G' of both the pastes were observed to be higher than the G" indicating dominating elastic behaviour when at rest. Further increase in the dynamic shear stress resulted in a

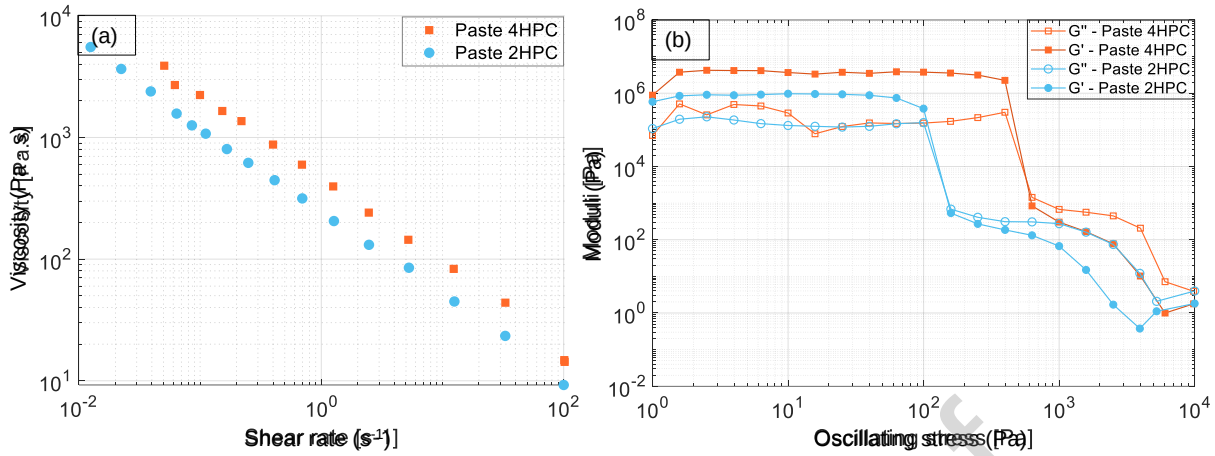

Figure 8 Rheological measurements of the different paste compositions: (a) flow sweeps obtained by rotational rheometry and (b) shear moduli as a function of shear stress obtained by oscillatory rheometry.

rapid drop of G' and G", on reaching a certain degree of the stress, which could be due to the abrupt damage in the structural network of the metal powder and the binder system causing the paste to flow. Liu et al. observed and reported similar behavior in the rheology of the alumina paste for extrusion-based printing [33]. The high G' and larger viscoelasticity limit for 4HPC paste compared to that of 2HPC could be attributed to the higher powder loading and higher amount of binder in the corresponding binder solution respectively. In addition, the flow points greater than 100 Pa for all pastes manifested good printability and stability of the parts on printing. The shear rates anticipated during the printing of the feedstock pastes were calculated, considering volumetric flow rate and radius of the nozzle (200 µm), to be in the range of 200-300 s^{-1}. However, it was observed that the measurement of viscosity by rotational rheometry using parallel plates geometry is limited to 100 s^{-1} as the paste is expelled at higher rates from between the plates resulting in an inaccurate outcome. Therefore, extrapolating the data to higher shear rates could be an approach to estimate an approximate viscosity and link to the printing process.

3.2 Selection of the printing parameters and feedstock paste

Table 2 reports the sintered density, in the range of 95.6 - 98.8 %, of the samples printed using the respective parameter combinations. The part density tends to decrease with increasing layer thickness and scan spacing. However, it was observed that the printing window for 3D micro-extrusion of dense components is substantially wide with minimal variation (<1.5%) in the relative density, except for the extremes in the parameter combination i.e. SP350/LT300 and SP300/LT300. The highest density could be achieved by decreasing the scan spacing to 250 µm. However, printability challenges were encountered with excess material buildup during printing leading to increased surface roughness (hence, only one part was printed and tested). Therefore, considering the aspects such as printability, excess material deposition, relative density, and geometrical properties, the combination of SP300/LT200 was selected for further printing and characterization (Table 3).

From the three-point bending tests, the load of rupture was measured to calculate the green strength of the parts shaped using 2HPC and 4HPC paste compositions. The 2HPC paste exhibited a green strength of 0.06 ± 0.00 MPa, whereas the 4HPC paste resulted in a green strength of 0.17 ± 0.01 MPa. Therefore, the 4HPC binder composition was chosen for printing the components for electrical and mechanical characterization.

Table 2 Relative density (%TD) of sintered pure Cu samples: different printing parameter combinations in terms of scan spacing (SP) and layer thickness (LT) were tested using a 400 µm nozzle with 4HPC paste (indicates that only one sample was printed per condition).*

SP↓/LT→ (µm)	200	225	250	300
350	98.13 ± 0.40	97.55 ± 0.14	97.19 ± 0.09	96.83*
300	97.62 ± 0.03	98.01 ± 0.24	97.25 ± 0.06	95.61 ± 0.22
250	98.77*	98.26*	98.52 ± 0.24	-

Table 3 Overview of printing parameters used in the present work for 3D micro-extrusion of copper with both feedstock pastes 2HPC and 4HPC.

Parameter	Units	Value
Nozzle diameter	µm	580 and 400
Printing speed	mm/s	20
Paste flow rate	g/min	0.7-1.0
Fiber orientation	-	Unidirectional hexagonal
Scan spacing	µm	400 (580 µm nozzle) and 300 (400 µm nozzle)
Layer thickness	µm	~50% of nozzle diameter

3.3 Chemical analysis

Table 4 compares the results from the chemical analysis conducted on the starting Cu powders and the sintered parts produced via 3D micro-extrusion. The Cu powders showed levels of impurities below 50 ppm except for oxygen with a concentration of 2600 ppm. On the other hand, for the sintered Cu part an O level of 17 ppm was measured highlighting the efficiency of the post-processing conditions in reducing the oxides. Moreover, a nearly complete removal of the organic additives was observed.

Table 4 Chemical analysis results of the starting pure Cu powder and sintered Cu part produced via 3D micro-extrusion.

Element	C (ppm)	O (ppm)	H (ppm)	N (ppm)
Cu powder	44	2600	42	5
Sintered part	170	17	2.6	1.8

3.4 Density and microstructural characterization of as-sintered condition

Table 5 Relative density (% TD) obtained through Archimedes measurement of as-sintered Cu samples (indicates that the error bar was calculated by measuring one sample multiple times).*

Sample No.	Nozzle Ø (µm)	Relative density (%TD)
2HPC_fiber	-	98.4 ± 0.09
2HPC_cuboid	580	97.8 ± 0.08*
4HPC_fiber	-	97.2 ± 0.25
4HPC_cuboid-1	580	98.19 ± 0.3
4HPC_cuboid-2	400	94.86 ± 0.34
4HPC_bar-1	580	95.72
4HPC_bar-2	400	98.77
4HPC_bar-3	400	96.83

97.11±1.26

Figure 9 and Figure 11 show the microstructural analysis on the cross-sections parallel (x-z) and perpendicular (y-z) to the printing direction respectively of a cuboid part printed with paste 2HPC (2HPC_cuboid in Table 5) and sintered to a relative density of 97.8 %. The part was printed with a 580 µm nozzle diameter employing the printing parameters listed in Table 3. The microstructures confirm the high density revealing no printing defects but a few micrometer sized (< 10 µm) residual pores after sintering homogeneously distributed throughout the sample. A higher magnification image (Figure 10) reveals the location of the residual porosity to be inter- and intragranular and at triple points similar to that of the sintered paste (Figure 7f). However, Figure 11 shows the occurrence of random defects within the printed parts that could be generated due to various reasons, like local instabilities in the feedstock paste.

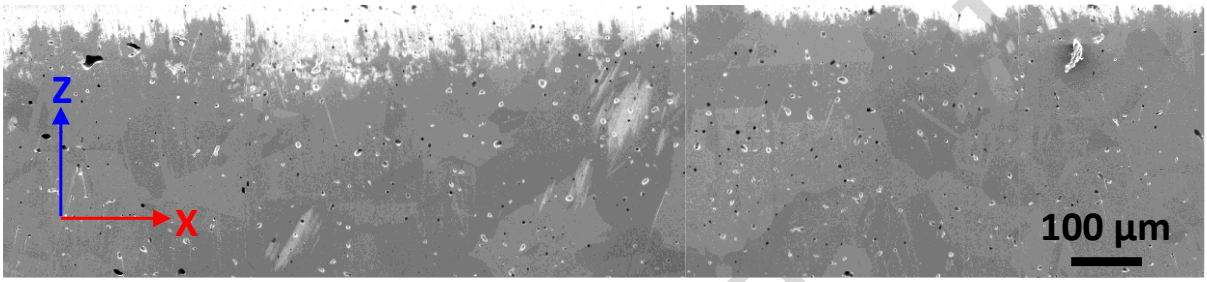

Figure 9 Microstructure of the cross-section parallel (x-z) to the printing direction of the part 2HPC_cuboid (Table 5) sintered to 97.8% TD.

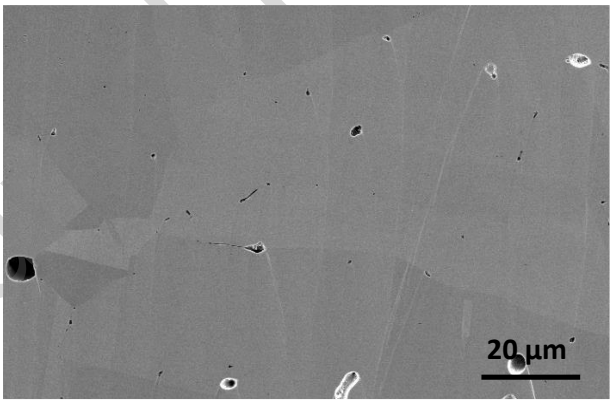

Figure 10 Higher magnification micrograph of the polished x-z section of 2HPC_cuboid.

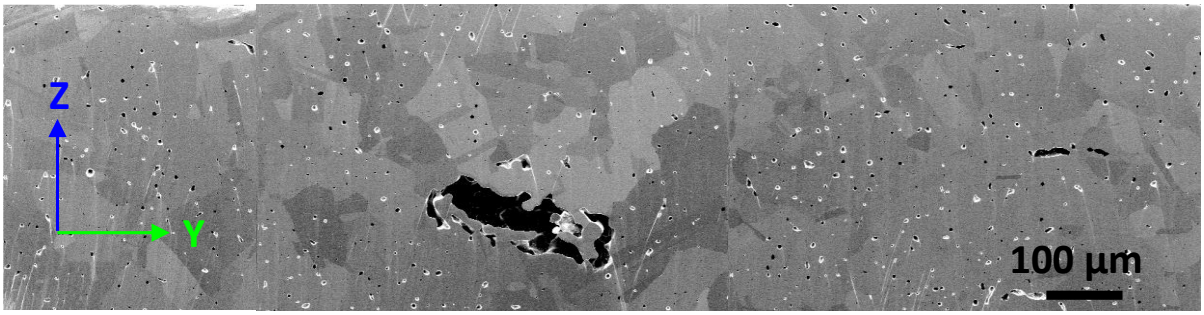

Figure 11 Microstructure of the cross-section perpendicular (y-z) to the printing direction of the part 2HPC_cuboid (Table 5) sintered to 97.8% TD.

A similar microstructural analysis was performed on 4HPC_cuboid-2, sintered to a relative density of 94.86 %. The part was printed using a nozzle of 400 µm diameter employing the printing parameters in Table 3. Figure 12 illustrates the microstructural features of the cross-section perpendicular to the printing direction. The microstructure revealing the presence of periodically aligned irregular porosity together with spherical residual porosity confirms the relatively lower density of this part. As the distance between the pores along the printing and build directions correlate with the printing parameters, these periodic porosities are attributed to non-optimal printing parameters (insufficient overlap and layer thickness), and can be classified as printing defects. However, the tensile bar 4HPC_bar-2, printed by employing similar printing parameters, had a high relative density of 98.8 %TD (Table 5). The major difference between the two printing conditions is the extrusion air pressure and thus paste flow rate. Part 4HPC_cuboid-2 (94.86 %TD) was printed with a relatively lower extrusion pressure and thus lower paste flow rate relative to the printing speed which might have resulted in an insufficient overlap of the extruded fibers and infill leading to interfiber defects in the green part. These defects emerged as printing-induced porosity that could not be densified by pressureless sintering. Figure 12 also shows the presence of periodically aligned pores at the bottom of the part. These are believed to be appearing as a result of similar non-optimum stacking of the fibers. The larger dimensions could be due to an additional influence of substrate and paste wetting at the bottom, unlike the paste-paste wetting beyond the first deposited layer.

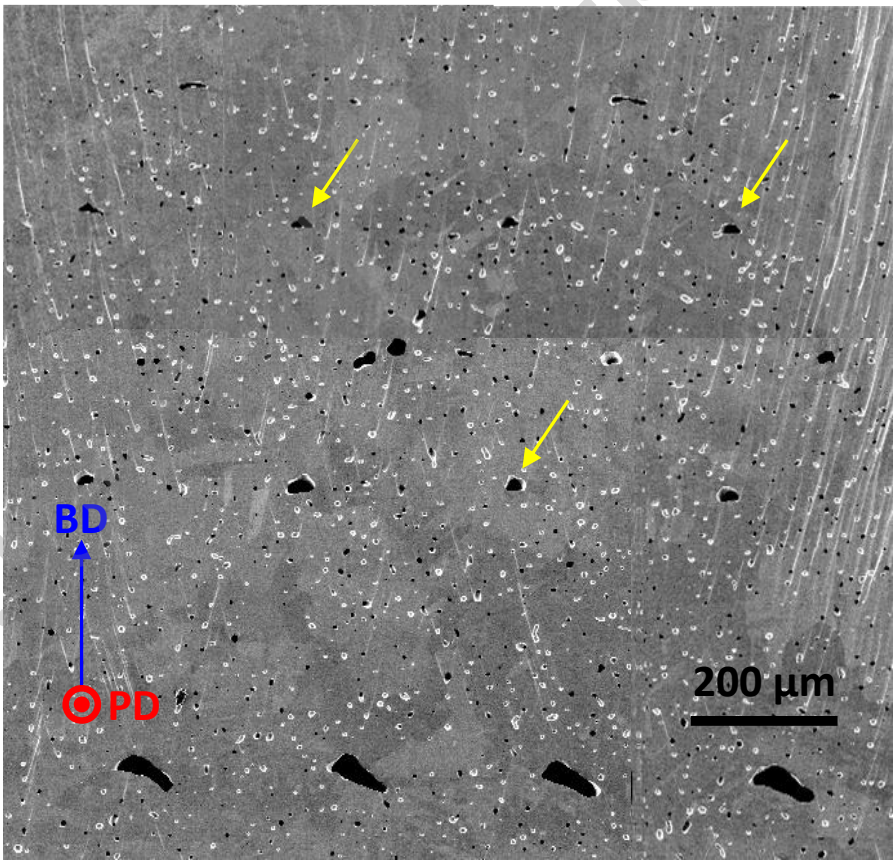

Figure 12 Microstructure of the cross-section perpendicular to the printing direction of the part 4HPC_cuboid-2 (Table 5) sintered to a relative density of 94.8%. The arrows in yellow indicate the presence of printing defects.

3D micro-extrusion of the two formulated feedstock pastes (2HPC and 4HPC) enabled the fabrication of pure Cu parts with sintered density in the range of 95-99 %TD. The microstructural characterization of the parts that were sintered to a relative density lower than 97 % showed the presence of periodic

printing induced defects. Only distributed isolated spherical pores were observed in the parts with final sintered density above 97 %.

3.5 Electrical conductivity measurements

Table 6 reports the electrical conductivity (% IACS), measured on the machined Cu parts, along with their corresponding relative density. The parts exhibited an electrical conductivity in the range of 98-100 %IACS, except for one part which delivered a relatively lower conductivity of 91.7 %IACS despite the high density of 98.7 %TD. 4HPC_cuboid-1 samples, with a relative density of 98.19 %TD, had a 98.3 %IACS conductivity obtained from probe measurement along the building direction (thickness). The bar shaped parts with a relative density in the range 95.7-98.7 %TD, measured for conductivity along the printing direction through 4-point contact method, delivered values in the range 91.7-100 %IACS. Both methods delivered similar electrical conductivity values, highlighting an isotropic conductivity. The pure Cu parts manufactured via 3D micro-extrusion exhibited electrical conductivity properties superior to the ones reported for binder-jetted copper after HIP [16] and Cu components produced by LPBF [11] as shown in Figure 13. The lower electrical conductivity of the parts produced by the latter technology was attributed to the presence of impurities [11]. However, the major impurities i.e. 170 ppm of C and 17 ppm of O (Table 4) in the 3D micro-extruded Cu parts do not seem to be detrimental for the electrical conductivity that was measured to be up to 100 %IACS.

Figure 13 shows a map of the density and electrical conductivity of additively manufactured Cu components by direct (LPBF [9,11] and EBM [12,14]) and indirect processes (BJ [15] and MEX [21,22], including the present work). The material properties achieved in the present work are comparable to those of pressure-assisted sintering conditions as well as direct AM processes.

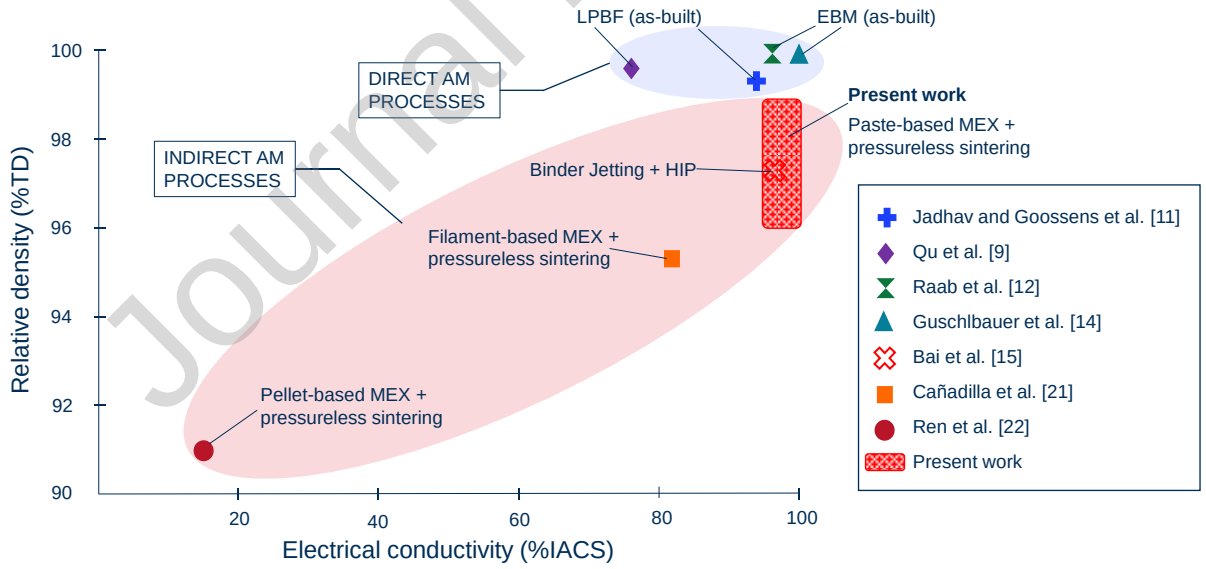

Figure 13 Density – conductivity map for direct (single-step) and indirect (multi-step) additively manufactured Cu components.

*Table 6 Relative density (%TD), electrical conductivity (%IACS) and tensile properties (E-modulus, YS, UTS and elongation %) measured for Cu parts produced via 3D micro-extrusion, compared to filament based MEX, L-PBF and wrought Cu literature data. (*E modulus not evaluated by IET)*

Sample	Relative density (%TD)	Electrical conductivity (%IACS)	Young's Modulus (GPa)	Yield strength (MPa)	Ultimate tensile strength (MPa)	Elongation (%)	Hardness (HV)
4HPC_cuboid -1	98.19 ± 0.21	98.30 ± 0.30	-	-	-	-	55.10 ± 0.10
4HPC_bar-1	95.72	99.83 ± 0.78	111	54.09	183.48	29	-
4HPC_bar-2	98.77	91.70 ± 0.45	123	67.18	201.67	35	-
4HPC_bar-3	96.84	100.65 ± 1.08	91*	61.44	196.00	33	-
Filament-based MEX [21]	95.30 ± 0.5	82.00	-	65.0 ± 1.5	205.80 ± 5.0	35.10 ± 1.4	54.80 ± 2.1
LPBF [11]	99.30	94 ± 1	-	122 ± 1	211 ± 4	43 ± 3	66 ± 1
Wrought Cu (C10100) [34]		≤102	115-132	69-365	221-455	4-55	51-104

3.6 Mechanical properties (IET and tensile testing)

Table 6 summarizes the mechanical properties of the sintered 3D micro-extruded parts after machining along with the relative density and electrical conductivity. It also compares the properties of 3D micro-extruded parts to other manufacturing process; MEX (Filament-based) [21], LBPF [11] and wrought copper [34]. The E modulus of the pure Cu bars were tested by IET on bar-shaped parts 4HPC_bar-1 and 2, whereas the bar-3 part was evaluated by tensile testing. The Young's modulus varied between 91 GPa and 123 GPa following the same trend as the corresponding relative density, i.e., a decrease in residual porosities resulted in a higher stiffness. The parts exhibited an yield strength (YS) of 61 ± 7 MPa, an ultimate tensile strength (UTS) of 194 ± 9 MPa and an elongation of 32 ± 4 %. The substantial elongation beyond the yield point prior to fracture on reaching ultimate tensile strength indicates significant amount of strain hardening. Upon reaching the UTS, the specimen did not demonstrate significant necking or gradual decrease in the stress, as in the case of conventional and LPBF processed copper [11]. On the contrary, a sharp drop in the stress-strain curve was observed demonstrating a combination of ductile and brittle fracture modes during the early and the last stages respectively. A similar behaviour was reported by Cañadilla et al. [21] for pure Cu parts produced by filament-based MEX. As illustrated in Table 6, the 3D micro-extruded parts showed comparable mechanical properties to filament-based MEX parts despite the difference in the relative density, microstructure and porosity (type, distribution, and morphology).

Figure 14 shows the fracture surface of one of the tensile bars (4HPC_bar-1) at different magnifications. A lower magnification micrograph (Figure 14a) reveals three main features: (i) the presence of dimples indicating a ductile fracture which is clearly demonstrated in Figure 14b-c, (ii) a region of poor densification (marked in blue) which could be a random defect generated during printing or in the paste, (iii) the printing-induced periodically aligned porosity (marked in red and shown in Figure 14b at a

higher magnification). This last feature could be related to the relative density of the tested part below 97 %TD. Additionally, the fracture surface revealed the presence of distributed isolated pores which are intrinsic of the sintering-based AM processes. The fracture mode and morphology of the fracture surface observed were partially similar to the analysis made on the tensile pure copper specimens produced by LBPF [11]. However, in contrast to 3D micro-extruded Cu parts, no evidence of distributed porosity was reported by Jadhav et al. This difference in microstructural features could be responsible for the lower YS obtained in the present study compared to that of LBPF (Table 6), and may also account for the lack of necking and brittle fracture in the last stage. Nevertheless, the UTS of LPBF (211 MPa) was comparable to 3D micro-extrusion [11]. The Cu parts produced via 3D micro-extrusion demonstrated mechanical properties in the range reported for a 99.99% pure Cu grade (C10100) produced via conventional manufacturing methods [34].

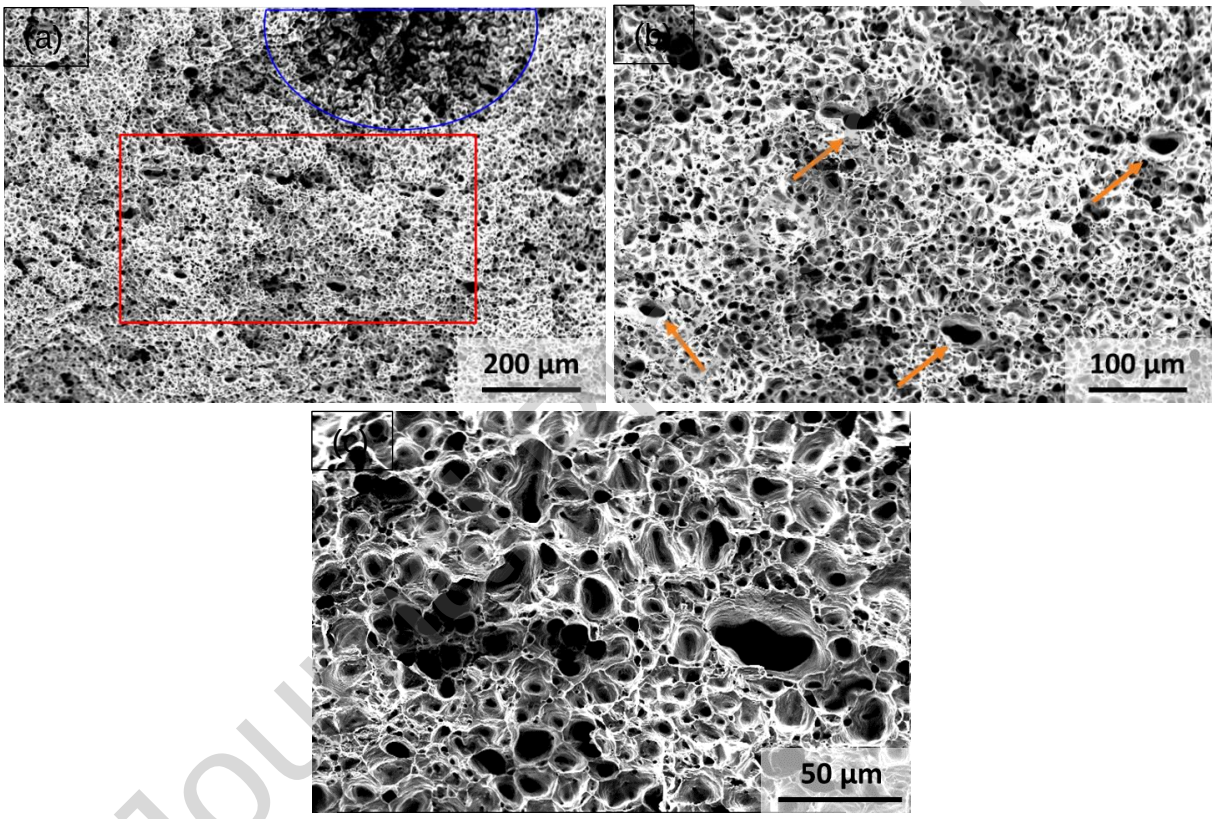

Figure 14 Micrographs of fracture surface of the tensile specimen obtained using SEM at (a) low different magnification, (b) and (c) at higher magnifications showing printing defects (indicated by orange arrows) and dimple fracture morphology respectively.

4. Conclusions

The present study focused on the development of a paste-based 3D micro-extrusion technology as a complete processing route to produce dense pure Cu parts. Two feedstock paste formulations were tested for 3D micro-extrusion to assess the impact of the binder content on the rheological behavior of the feedstock material and the strength of the green parts after printing. Degassing was identified to be a crucial step to eliminate large spherical gas inclusions and to achieve a dense feedstock paste. Assessment of the printing parameters revealed that the 3D micro-extrusion technology allows a broad printing window. The post-processing treatment consisted of a thermal debinding at 550°C/5h in

Ar+5H_2 atmosphere followed by pressureless sintering at 1050°C/5h in pure H_2 gas. An exceptionally high relative density in the range of 96-99% could be achieved by this technology compared to the other indirect AM technologies, irrespective of the two different paste compositions employed. For parts sintered to a relative density superior to 97%TD, the microstructural characterization revealed a dense cross-section with micrometric-sized closed spherical residual pores distributed inside the grains, at the grain boundaries and at triple junctions. Printing-induced porosity is detected in specimens with relative density below 97%. The sintered parts exhibited an outstanding electrical conductivity up to 100% IACS. This indicates the negligible impact of the low levels of impurities (170 ppm of O and 17 ppm of C) and the residual porosity after sintering on the electrical conductivity. The parts with a residual porosity ranging from 4.3 to 1.2 % demonstrated a Young's modulus between 111 and 123 MPa respectively. The sintered parts had a tensile yield strength, tensile strength and elongation of 61 ± 7 MPa, 194 ± 9 MPa and 32 ± 4 % respectively with a combination of ductile and brittle fracture modes. The latter could be attributed to the presence of distributed residual porosity after sintering.

Acknowledgements

This research was partially financed by the Flemish Research Foundation (FWO) in project (S001721N) entitled Multi-Material Additive Manufacturing for Electrical Machines with increased performance (AM4EM). S. Kolli thanks Vito for her research fellowship. The authors thank Aurubis Olen NV for the single probe electrical conductivity measurements.

References

[1] R.K. Shah, B. Thonon, D.M. Benforado, Opportunities for heat exchanger applications in environmental systems, Appl Therm Eng. (2000) 631–650.

[2] G. Lei, J. Zhu, Y. Guo, Multidisciplinary Design Optimization Methods for Electrical Machines and Drive Systems, Springer, 2016.

[3] R. Wrobel, B. Mecrow, A Comprehensive Review of Additive Manufacturing in Construction of Electrical Machines, IEEE Transactions on Energy Conversion. 35 (2020) 1054–1064. https://doi.org/10.1109/TEC.2020.2964942.

[4] T.J. Horn, D. Gamzina, Additive Manufacturing of Copper and Copper Alloys, in: Additive Manufacturing Processes, ASM International, 2020: pp. 388–418. https://doi.org/10.31399/asm.hb.v24.a0006579.

[5] M. Norfolk, H. Johnson, Solid-State Additive Manufacturing for Heat Exchangers, JOM. 67 (2015) 655–659. https://doi.org/10.1007/s11837-015-1299-6.

[6] S.D. Jadhav, S. Dadbakhsh, L. Goossens, J.-P. Kruth, J. van Humbeeck, K. Vanmeensel, Influence of selective laser melting process parameters on texture evolution in pure copper, J Mater Process Technol. 270 (2019) 47–58.

[7] S. Gruber, L. Stepien, E. López, F. Brueckner, C. Leyens, Physical and geometrical properties of additively manufactured pure copper samples using a green laser source, Materials. 14 (2021). https://doi.org/10.3390/ma14133642.

[8] S.D. Jadhav, J. Vleugels, J.P. Kruth, J. Van Humbeeck, K. Vanmeensel, Mechanical and electrical properties of selective laser-melted parts produced from surface-oxidized copper powder, Material Design and Processing Communications. 2 (2020). https://doi.org/10.1002/mdp2.94.

[9] S. Qu, J. Ding, J. Fu, M. Fu, B. Zhang, X. Song, High-precision laser powder bed fusion processing of pure copper, Addit Manuf. 48 (2021). https://doi.org/10.1016/j.addma.2021.102417.

[10] X. Yan, C. Chang, D. Dong, S. Gao, W. Ma, M. Liu, H. Liao, S. Yin, Microstructure and mechanical properties of pure copper manufactured by selective laser melting, Materials Science and Engineering A. 789 (2020). https://doi.org/10.1016/j.msea.2020.139615.

[11] S.D. Jadhav, L.R. Goossens, Y. Kinds, B. Van Hooreweder, K. Vanmeensel, Laser-based powder bed fusion additive manufacturing of pure copper, Addit Manuf. 42 (2021). https://doi.org/10.1016/j.addma.2021.101990.

[12] S.J. Raab, R. Guschlbauer, M.A. Lodes, C. Körner, Thermal and Electrical Conductivity of 99.9% Pure Copper Processed via Selective Electron Beam Melting, Adv Eng Mater. 18 (2016) 1661–1666. https://doi.org/10.1002/adem.201600078.

[13] M.A. Lodes, R. Guschlbauer, C. Körner, Process development for the manufacturing of 99.94% pure copper via selective electron beam melting, Mater Lett. 143 (2015) 298–301. https://doi.org/10.1016/j.matlet.2014.12.105.

[14] R. Guschlbauer, S. Momeni, F. Osmanlic, C. Körner, Process development of 99.95% pure copper processed via selective electron beam melting and its mechanical and physical properties, Mater Charact. 143 (2018) 163–170. https://doi.org/10.1016/j.matchar.2018.04.009.

[15] Y. Bai, C.B. Williams, An exploration of binder jetting of copper, Rapid Prototyp J. 21 (2015) 177–185. https://doi.org/10.1108/RPJ-12-2014-0180.

[16] A. Yegyan Kumar, J. Wang, Y. Bai, S.T. Huxtable, C.B. Williams, Impacts of process-induced porosity on material properties of copper made by binder jetting additive manufacturing, Mater Des. 182 (2019). https://doi.org/10.1016/j.matdes.2019.108001.

[17] G. Singh, P.M. Pandey, Rapid manufacturing of copper components using 3D printing and ultrasonic assisted pressureless sintering: Experimental investigations and process optimization, J Manuf Process. 43 (2019) 253–269. https://doi.org/10.1016/j.jmapro.2019.05.010.

[18] N. Sa'ude, M. Ibrahim, M. Ibrahim, M. Wahab, R. Haq, O. Marwah, R. Khirotdin, Additive Manufacturing of Copper-ABS Filament by Fused Deposition Modeling (FDM), Journal of Mechanical Engineering. 5 (2018) 23–32.

[19] E. Redondo, M. Pumera, Fully metallic copper 3D-printed electrodes via sintering for electrocatalytic biosensing, Appl Mater Today. 25 (2021). https://doi.org/10.1016/j.apmt.2021.101253.

[20] M. Sadaf, S. Cano, J. Gonzalez-Gutierrez, M. Bragaglia, S. Schuschnigg, C. Kukla, C. Holzer, L. Vály, M. Kitzmantel, F. Nanni, Influence of Binder Composition and Material Extrusion (MEX) Parameters on the 3D Printing of Highly Filled Copper Feedstocks, Polymers (Basel). 14 (2022). https://doi.org/10.3390/polym14224962.

[21] A. Cañadilla, A. Romero, G.P. Rodríguez, M. Caminero, Ó.J. Dura, Mechanical, Electrical, and Thermal Characterization of Pure Copper Parts Manufactured via Material Extrusion Additive Manufacturing, Materials. 15 (2022). https://doi.org/10.3390/ma15134644.

[22] L. Ren, X. Zhou, Z. Song, C. Zhao, Q. Liu, J. Xue, X. Li, Process parameter optimization of extrusion-based 3D metal printing utilizing PW-LDPE-SA binder system, Materials. 10 (2017). https://doi.org/10.3390/ma10030305.

[23] G. Singh, J.-M. Missiaen, D. Bouvard, J.-M. Chaix, Copper additive manufacturing using MIM feedstock: adjustment of printing, debinding, and sintering parameters for processing dense and defectless parts, (n.d.). https://doi.org/10.1007/s00170-021-07188-y/Published.

[24] S. Danaci, L. Protasova, F. Snijkers, W. Bouwen, A. Bengaouer, P. Marty, Innovative 3D-manufacture of structured copper supports post-coated with catalytic material for CO2 methanation, Chemical Engineering and Processing - Process Intensification. 127 (2018) 168–177. https://doi.org/10.1016/j.cep.2018.03.023.

[25] X. Yan, C. Wang, W. Xiong, T. Hou, L. Hao, D. Tang, Thermal debinding mass transfer mechanism and dynamics of copper green parts fabricated by an innovative 3D printing method, RSC Adv. 8 (2018) 10355–10360. https://doi.org/10.1039/c7ra13149f.

[26] S. Hong, C. Sanchez, H. Du, N. Kim, Fabrication of 3D Printed Metal Structures by Use of High-Viscosity Cu Paste and a Screw Extruder, J Electron Mater. 44 (2015) 836–841. https://doi.org/10.1007/s11664-014-3601-8.

[27] U.K. Roopavath, S. Malferrari, A. van Haver, F. Verstreken, S.N. Rath, D.M. Kalaskar, Optimization of extrusion based ceramic 3D printing process for complex bony designs, Mater Des. 162 (2019) 263–270. https://doi.org/10.1016/j.matdes.2018.11.054.

[28] E. Udofia, E.N. Udofia, W. Zhou, Microextrusion Based 3D Printing-A Review Production of 3-D Geometric Models with Aluminium Scraps Using CAD/CAM Systems View project Microheater Array Powder Sintering View project Microextrusion Based 3D Printing-A Review, n.d. https://www.researchgate.net/publication/335430080.

[29] R. Côté, V. Demers, N.R. Demarquette, S. Charlon, J. Soulestin, A strategy to eliminate interbead defects and improve dimensional accuracy in material extrusion 3D printing of highly filled polymer, Addit Manuf. 68 (2023). https://doi.org/10.1016/j.addma.2023.103509.

[30] E. Feilden, E.G.T. Blanca, F. Giuliani, E. Saiz, L. Vandeperre, Robocasting of structural ceramic parts with hydrogel inks, J Eur Ceram Soc. 36 (2016) 2525–2533. https://doi.org/10.1016/j.jeurceramsoc.2016.03.001.

[31] H. Tiismus, A. Kallaste, T. Vaimann, A. Rassõlkin, State of the art of additively manufactured electromagnetic materials for topology optimized electrical machines, Addit Manuf. 55 (2022). https://doi.org/10.1016/j.addma.2022.102778.

[32] L. del-Mazo-Barbara, M.P. Ginebra, Rheological characterisation of ceramic inks for 3D direct ink writing: A review, J Eur Ceram Soc. 41 (2021) 18–33. https://doi.org/10.1016/j.jeurceramsoc.2021.08.031.

[33] H. Liu, Y. Li, D. Li, Research on rheological properties and extrusion behavior of aqueous alumina paste in paste-extrusion-based SFF processes, International Journal of Advanced Manufacturing Technology. 83 (2016) 2039–2047. https://doi.org/10.1007/s00170-015-7720-z.

[34] J.R. Davis, ASM Specialty Handbook Copper and Copper Alloys, ASM International, 2001. www.asminternational.org.

Author Statement

Margherita Beretta: Investigation, Methodology, Writing- Original draft, Writing- Reviewing and Editing

Samanwitha Kolli: Investigation, Methodology, Writing- Original draft, Writing- Reviewing and Editing

Ahmed Selema: Investigation, Methodology, Writing- Reviewing and Editing

Peter Sergeant: Conceptualization, Funding acquisition, Project administration, Resources, Supervision, Validation, Writing- Reviewing and Editing

Leo A.I. Kestens: Conceptualization, Funding acquisition, Project administration, Resources, Supervision, Validation, Writing- Reviewing and Editing

Marleen Rombouts: Conceptualization, Funding acquisition, Project administration, Resources, Supervision, Validation, Visualization, Writing- Reviewing and Editing

Jozef Vleugels: Conceptualization, Funding acquisition, Project administration, Resources, Supervision, Validation, Visualization, Writing- Reviewing and Editing

Declaration of interests

☒ The authors declare that they have no known competing financial interests or personal relationships that could have appeared to influence the work reported in this paper.

☐ The authors declare the following financial interests/personal relationships which may be considered as potential competing interests: